

Three-Dimensional Thermocline Dynamics in Thermal Storage Tanks

S. S. Ratnu and K. V. Manu[†]

*Department of Aerospace Engineering, Indian Institute of Space Science and Technology,
 Thiruvananthapuram, 695547, Kerala, India*

[†]*Corresponding Author Email: manukv@iist.ac.in*

(Received August 28, 2020; accepted March 14, 2021)

ABSTRACT

In this work, a series of three-dimensional unsteady numerical simulations are performed to study the stability and interface dynamics of a thermocline-based lab-scale single tank Thermal Energy Storage system (TES). The stability of thermocline is analysed by introducing relatively cold fluid for a short period at the inlet of the TES. Numerical simulations are performed for three inlet flow disturbances (weak, medium and strong) and three stratification levels (sharp, moderate and large). The fluid injected at the inlet rolls-up and interacts with the thermocline which causes spatio-temporal disruption of the stable stratification inside the TES. It was found that the three-dimensional simulations bear some resemblance to the two-dimensional case but also show crucial differences. The propagation of the injected cold fluid and the subsequent interaction with the thermocline are analysed. A wide gamut of flow structures is identified inside the TES depending on the degree of stratification and level of disturbance. Finally, the oscillatory nature of interface and associated mixing mechanism are addressed. The simulation indicates that the oscillations at the interface are through the successive generation of countersign vorticity which retards/suppresses the propagation of the vortex ring. In the case of large interface, internal waves are generated by the periodic array of vortices which generates a standing wave pattern near the Brunt-Väisälä frequency.

Keywords: Stratified storage system; Vorticity dynamics; Baroclinicity; Buoyancy frequency.

NOMENCLATURE

A	atwood number	t	flow Time
C_p	specific heat	V	axial component of velocity
D	diameter of the tank	x	axial distance of the pipe
p	pressure	δ	thermocline thickness
h	height of the tank	Γ	circulation
r	radial distance from center of pipe	ν	kinematic viscosity
R	radius of the pipe	ρ	density of the fluid
k	thermal conductivity	τ	non-dimensional time scale for starting flows
N	buoyancy frequency	Subscript	
Re	Reynolds number	c	cold-fluid properties
Ri	Richardson number	h	hot-fluid properties
T	temperature	d	disturbance fluid properties

1. INTRODUCTION

Concentrated solar power (CSP) systems are affordable, eco-friendly energy technology for large-scale conversion of solar energy to electricity. CSP systems can generate uninterrupted electricity on demand through the efficient use of thermal energy

storage systems ([Medrano et al. 2010](#); [Gil et al. 2010](#)). It has been identified that the cost of storage systems can be minimized up to 35% by storing the hot and cold fluid in a single-tank system in stratified configuration ([Yang and Garimella 2010](#); [Kearney et al. 2003](#)). However, maintaining a stable stratification under various operating conditions is one of the major challenges associated with single

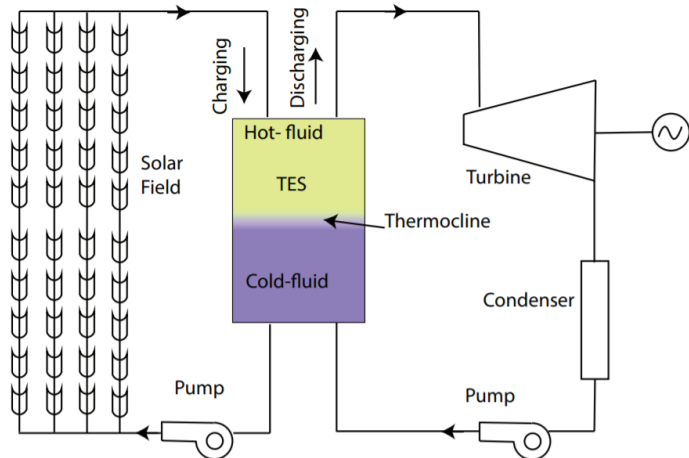


Fig. 1. Schematic of thermocline storage concept.

tank TES. The implementation of molten tank based single tank TES system and associated strategies are discussed in the recent experimental works of [Yuan et al. \(2018\)](#) and [Advaith et al. \(2021\)](#).

In a single tank thermocline storage system the less dense hot-fluid is stored above the denser cold fluid in stratified configuration (Fig. 1). A complete storage process in a single tank TES involves mainly three process: charging, storing and discharging. During the charging process, hot fluid from the solar collection field enters into the tank from the top and forces out the existing cold fluid from the bottom of the tank (Fig. 1), while during the discharging process, hot fluid from the top, pumps to the power block to generate electricity and re-enters from the bottom at a comparatively less temperature. These processes cause heat exchange between hot and cold of the fluid resulting the formation of high temperature gradient region known as ‘thermocline’. Theoretically, in a TES, the hot fluid sits at the top-half while the cold fluid positioned at the bottom-half of the tank. Extensive review regarding the working and performance of molten salt based TES can be found in [González-Roubaud et al. \(2017\)](#) and [Suresh and Saini \(2020\)](#).

Different heat and mass transfer phenomena that occur in a TES can have an adverse effect on thermal stratification ([Qin et al. 2012](#)). For example, during the charging process, relatively cold fluid can enter the TES due to the diurnal variation of solar radiation. This can cause distortion of thermal stratification and undesirable mixing of hot and cold fluid inside the TES. The entrainment of cold fluid into hot fluid can cause an increase in the thermocline thickness thereby affecting the stratification efficiency. Quantitative comparison of instabilities that occurred in two dimensional and three dimensional simulations are performed by [Van Berkel et al. \(2002\)](#) in a thermocline based water storage tank. In two-dimensional simulations the entrainment velocity was 40% higher than that found in the corresponding three dimensional simulations. Also, a higher level of internal waves and more kinetic energy is present at large scales in two-

dimensional simulations. They have observed Kelvin-Helmholtz-like waves in the three dimensional simulations.

For high temperature CSP applications, molten salt, (a eutectic mixture of sodium and potassium nitrate) are commonly employed as heat transfer fluid (HTF) ([Reddy 2011](#)). Compared with other organic HTF, molten salt allows wider working temperature range, efficient thermal stability and relatively low vapor pressure. Recently, a series of two-dimensional Computational Fluid Dynamics (CFD) studies were conducted to study the impact of various hydrodynamic instabilities and associated mixing in a molten salt based lab-scale TES ([Manu et al. 2015](#); [Manu et al. 2016](#); [Hatte et al. 2016](#); [Tinaikar et al. 2016](#)). Characteristic flow features of Rayleigh-Taylor (RT) instabilities such as bubble and spike-like structures are observed in the numerical simulations of [Manu et al. \(2016\)](#). The effects of Atwood number and Froude number on the thermocline mixing dynamics induced by RT instabilities are analysed by [Manu et al. \(2015\)](#). The transient nature of thermocline under subsequent cyclic charging-discharging are analysed by [Hatte et al. \(2016\)](#). In an interesting work, [Tinaikar et al. \(2016\)](#) experimentally and numerically analysed the mixing dynamics induced by successive laminar vortex pairs. [Tinaikar et al. \(2016\)](#) observed that the flow features of thermocline under external perturbations are analogous to the vortex-stratified interface interactions experiments ([Linden 1973](#); [Dahm et al. 1989](#); [Orlandi et al. 1998](#)).

[Dahm et al. \(1989\)](#) posited that for thin interfaces, baroclinic production and topology of the vortices formed at the interface are governed by Atwood number and vorticity-based Froude number. However, in case of thick interface, the interaction mechanism and associated mixing are governed by thickness of the interface, distance between the vortices, Atwood number and Froude number. Recently, [Advaith et al. \(2017\)](#) conducted experiments on the interaction of vortex ring with a finite thickness stratified interface mimicking the thermocline-disturbance interaction observed in

TES. They have classified vortex ring interface mechanism into three regimes (non-penetrative, partially penetrative and extensively penetrative) based on maximum penetration length. The importance of three dimensional effects are revealed from the recent time-resolved stereoscopic Particle Image Velocimetry (stereo PIV) measurements of [Olstoorn and Dalziel \(2017\)](#). They have observed that the time scale associated with the instability growth decreases with increasing Richardson number. The effect of Pelet and the Atwood number on thermal stratification is reported by [Shaikh et al. \(2018\)](#).

In this work the stability of a molten salt based single TES is analysed for different flow configurations using CFD. The results are presented using important non-dimensional numbers. Hence the reported results can be easily ported to other types of storage as well. The goal of this work is to gain insight into the three dimensional transient dynamics of the thermocline and its stability which are consistent with the practical conditions. The effects of thermocline thickness on various flow features have been studied in detail.

This paper is organized as follows. The details of governing equations, boundary and initial conditions used for the present study are provided in sections 2.1 and 2.2. A grid independence analysis is given in section 2.3. In section 3, the flow physics behind the mixing mechanism have been analysed for nine flow conditions. Initially, the initial development of three types of disturbances is analysed (section 3.1). The interface mechanisms between a weak disturbance with sharp, moderate and large interface thickness levels are analysed in section 3.21. The interaction between a medium disturbance with sharp, moderate and large interface thickness levels are analysed in section 3.22. In section 3.23, the interaction between a strong disturbance with sharp, moderate and large interface thickness levels are analysed. Finally, oscillatory nature of the interface associated with baroclinic production of vorticity is analysed in section 3.3. The results are summarized in section 4.

2. NUMERICAL METHODOLOGY

TES is modelled as a cylindrical three-dimensional domain of diameter (D) 150 mm and height(h) 500 mm. The aspect ratio(h/d) for lab scale geometry used is 3.34, which is the comparable with that used in industrial applications. The schematic of computational domains with boundary conditions are shown in Figure 2. Here, x and z coordinates correspond to radial directions and y coordinate correspond to axial direction. Velocity in radial, axial directions are represented by u and v respectively. The properties of hot, cold and disturbance fluids are denoted by sub-scripts h, c and d respectively. The grid was generated by Pointwise V18R3.

2.1 Governing equations

A commercially available program ANSYS FLUENT 16.2 was used for solving transient three dimensional mass, momentum and energy conservation equation.

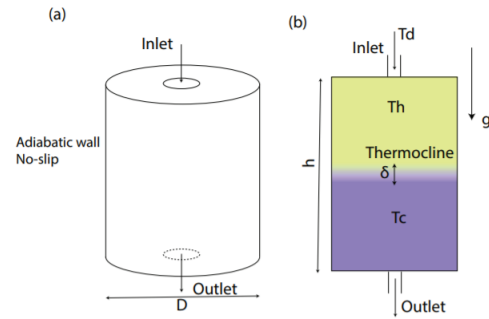


Fig. 2. Schematic of computational domain and boundary conditions:
(a) three dimensional view; (b) two-dimensional cross sectional view.

The governing equations are:

$$\frac{\partial \rho}{\partial t} + \nabla \cdot (\rho \vec{v}) = 0 \quad (1)$$

$$\frac{\partial(\rho \vec{v})}{\partial t} + \nabla \cdot (\rho \vec{v} \vec{v}) = -\nabla p + \nabla \cdot (\bar{\tau}) + \rho \vec{g} \quad (2)$$

$$\frac{\partial(\rho E)}{\partial t} + \nabla \cdot (\vec{v}(\rho E + p)) = \nabla \cdot (k \nabla T) \quad (3)$$

$$\text{Where } \bar{\tau} = \mu \left[\nabla \vec{v} + (\nabla \vec{v}^T) - \frac{2}{3} \nabla \cdot \vec{v} I \right]$$

$$E = h - \frac{p}{\rho}$$

FLUENT implements the SIMPLE algorithm for solving the Navier-Stokes equations for variable density flow. Spatial discretization of the convective fluxes is performed with a second-order upwind scheme. Body-force weighted scheme for pressure discretization was used to incorporate gravitational force terms and second order implicit scheme used for transient terms. The scaled absolute values of the residuals, for velocities and temperature, were set to 10^{-5} as convergence criteria for each time step. Under-relaxation factor of 0.3 and 0.7 were selected for pressure and momentum respectively. The time step used for the simulations is $\Delta t = 2 \times 10^{-3} \text{ s}$ so that the CFL number ($\frac{v \Delta t}{\Delta x}$) was kept below 0.1 for all the simulations. Molten salt (HITEC salt) with following thermo-physical properties [Xu et al. 2012](#) was used as the HTF

$$\rho(T) = 2090 - 0.636T(\text{°C}) \quad (4)$$

$$C_p(T) = 1443 - 0.172T(* \text{C}) \quad (5)$$

$$k(T) = 0.443 + 0.00019 T(\text{C}) \quad (6)$$

$$\begin{aligned} \mu(T) = & [22.714 - 0.12T + 2.281 \times 10^{-4}T^2 \\ & - 1.474 \times 10^{-7}T^3] \times 10^{-3}(\text{C}) \end{aligned} \quad (7)$$

2.2 Initial and boundary conditions

The velocity boundary condition is applied at the inlet and the outlet of the TES as in the two dimensional simulations of (Tinaikar *et al.* 2016). Adiabatic thermal condition is applied for the storage tank walls by setting a zero heat flux at the wall surface. At side walls, top plane and bottom plane (except inlet and outlet of domains) no-slip and adiabatic conditions are assigned.

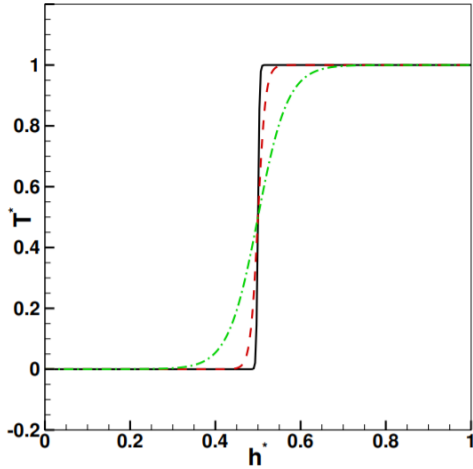


Fig. 3. Non-dimensional temperature profile (sigmoid function).

Temperature profile is initialized by the following sigmoid profile as shown in Fig. 3. This distribution of temperature at the end of the charging process can be represented by the sigmoid profile as shown in various studies (Zachar *et al.* 2003; Flueckiger *et al.* 2013).

$$T = T_c + \frac{T_h - T_c}{1 + e^{-m(y-n)}} \quad (8)$$

Here, m represents the shape parameter which determines the thermocline thickness and n designates the axial location of the thermocline. The thickness of thermocline calculated using the following expression

$$\delta = \delta_{Th} - \delta_{Tc}$$

Here, δ_{Th} is the lowest y value at which the temperature reached $0.99 T_h$ and δ_{Tc} is the largest value at which the temperature attains a value of $1.01 T_c$. Here, the values of T_h and T_c are 651K and 563K. Disturbances were introduced by adding the colder fluid at inlet through a port with a 7.5 mm (d) with Velocity V_d and temperature T_d into the stable thermocline which is maintained at the center of the tank. The temperature ($T_d = 610$) has temperature higher than cold fluid temperature and lower than hot fluid temperature($T_c < T_d < T_h$).

The disturbance velocity and temperature at inlet are as follows; for weak disturbance:

$$V_d = \begin{cases} 0.079 & 0 < t < 0.25s \\ 0 & t \geq 0.25s \end{cases} \quad (9)$$

$$T_d = \begin{cases} 610K & 0s < t < 0.25s \\ 651K & t \geq 0.25s \end{cases} \quad (10)$$

The disturbance velocity and temperature at inlet are as follow; for medium disturbance:

$$V_d = \begin{cases} 0.079 & 0s < t < 0.50s \\ 0 & t \geq 0.50s \end{cases} \quad (11)$$

$$T_d = \begin{cases} 610K & 0s < t < 0.50s \\ 651 & t \geq 0.50s \end{cases} \quad (12)$$

The disturbance velocity and temperature at inlet are as follows; for strong disturbance:

$$V_d = \begin{cases} 0.079 & 0s < t < 0.75s \\ 0 & t \geq 0.75s \end{cases} \quad (13)$$

$$T_d = \begin{cases} 610K & 0s < t < 0.75s \\ 651 & t \geq 0.75s \end{cases} \quad (14)$$

The following definitions are used to define Atwood number (A), Reynolds number(Re) and circulation based Reynolds number.

$$A = \frac{\rho_c - \rho_h}{\rho_c + \rho_h} \quad (15)$$

$$Re = \frac{\rho_d V_d}{\mu_d} \quad (16)$$

$$Re_v = \frac{\Gamma}{2\pi\nu} \quad (17)$$

Here, Γ is the circulation strength.

Here, in Eq. 16 the diameter of the pipe is selected as one of the length scales to define Reynolds number as during in many vortex-ring-induced stratified mixing studies Shy (1995), Olsthoorn and Dalziel (2017). However, in the present case, the inlet flow is discontinuous as evident in Eq. 9. Hence a better way to calculate the ratio of inertia and viscous force is to use circulation-based Reynolds number which is used in vorticity dominated flows. This alternate definition allows us to include the effect of flow duration as shown in many other experimental and numerical works Dahm *et al.* (1989), Orlandi *et al.* (1998). The following definitions are used to define Richardson number, Richardson number based of circulation and Froude number.

$$Ri = \frac{g(\rho_c - \rho_h)d}{\rho_h V_d^2} \quad (18)$$

$$Ri_v = AR \quad (19)$$

where, $R = a^3 g / \Gamma^2$

$$Fr = \frac{V_d}{Nd} \quad (20)$$

Table 1 Simulation details.

Case	$\tau_d(s)$	Re	Ri	δ/h	A	R	$Ri_v = AR$	Re_v	Fr
SC1	0.25	438	0.908	0.008	0.072	3.55	0.142	197.68	0.281
SC2	0.50	438	0.908	0.008	0.072	3.15	0.126	869.561	0.317
SC3	0.75	438	0.908	0.008	0.072	1.72	0.068	915.451	0.581
MC1	0.25	438	0.908	0.034	0.072	3.55	0.142	197.68	0.281
MC2	0.50	438	0.908	0.034	0.072	3.15	0.126	869.561	0.317
MC3	0.75	438	0.908	0.034	0.072	1.72	0.068	915.451	0.581
LC1	0.25	438	0.908	0.182	0.072	3.55	0.142	197.68	0.281
LC2	0.50	438	0.908	0.182	0.072	3.15	0.126	869.561	0.317
LC3	0.75	438	0.908	0.182	0.072	1.72	0.068	915.451	0.581

$$\text{where, } N = \sqrt{-\frac{g}{\rho_0} \frac{\partial \rho(y)}{\partial y}}$$

$$\text{and } \rho_0 = \frac{\rho_h + \rho_c}{2}$$

Here, a is the distance between two vortex centre. The non-dimensional numbers along with other parameters are tabulated in table 1.

2.3. Mesh Independent Analysis

A mesh independent analysis is conducted to determine the optimum grid to capture the flow physics. Initially, three types of meshes of sizes $254 \times 600 \times 254$ (Fine mesh), $127 \times 300 \times 127$ (medium mesh) and $64 \times 150 \times 64$ (coarse mesh) were considered for the simulations. Figure 4 shows the effect of grid resolution on temperature at $t^* = 0.47$. The difference between fine grid and medium grid is negligible. Here, the maximum difference in velocity and temperature are 1.2% and 3.00% respectively. Hence to reduce computational cost and time, grid $127 \times 300 \times 127$ (medium mesh) is considered for further simulations.

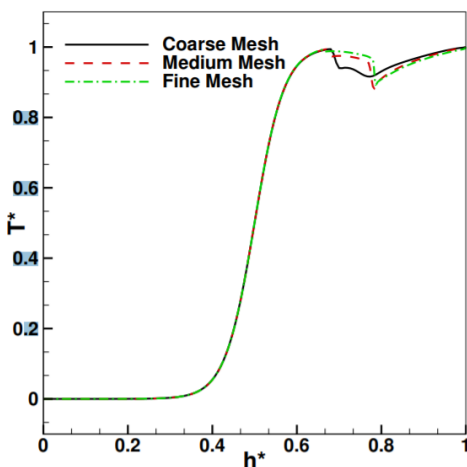


Fig. 4. Mesh independent analysis.

3. RESULTS

The two-dimensional view of the instantaneous non-dimensional temperature plots ($T^* = \frac{T - T_c}{T_h - T_c}$) at various non-dimensionalized time instance ($t^* = \frac{tV_d}{h}$) of weak disturbance cases (SC1, MC1 and LC1) are shown in Figs. 5 (a), (b) and (c). The evolution of the flow disturbance inside the TES happens in three distinct phases: the initial roll-up, vortex-thermocline interaction and recovery phase. During the initial phase, the added disturbance fluid rolls-up near the inlet port region ($t^* \approx 0.47$). The interface is unaffected by the added perturbation during the initial phase. Subsequently, in the second phase ($0.47 \leq t^* \leq 1.89$) the rolled up flow structure penetrates the lighter hot-fluid and impinges on the thermocline region.

Depending upon the interface thickness and strength of the disturbance, a wide gamut of flow patterns are formed near the thermocline region. This interaction mechanisms are analogous to the vortex ring-density interaction experiments of (Linden 1973; Dahm *et al.* 1989; Orlandi *et al.* 1998; Advaita *et al.* 2017) and various two dimensional simulations (Manu *et al.* 2015; Manu *et al.* 2016; Tinaikar *et al.* 2016). Unfortunately, to our knowledge no experimental data is available for direct comparison with Molten salt based TES.

In Fig. 6 the numerical simulations results are compared with the visualization experiments of (Dahm *et al.* 1989). As shown in the Fig. 6 for similar AR value ($AR \approx 0.1$) the flow features are similar with the the experimental observations of (Dahm *et al.* 1989). This interaction causes oscillation of thermocline region. Finally, during the recovery phase ($t^* \geq 1.89$), thermocline oscillations are observed and a new thermocline with increased thickness is established.

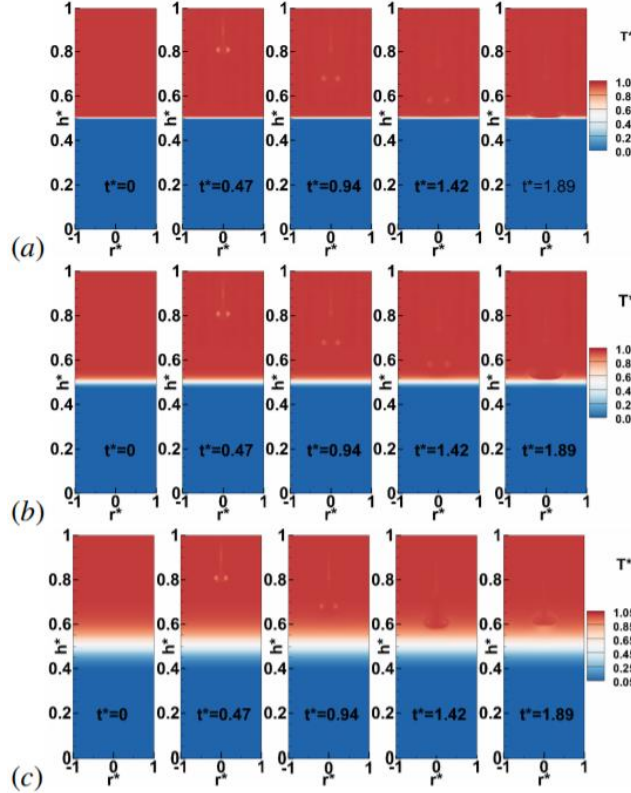


Fig. 5. Temperature contour at different flow instances; case SC1.

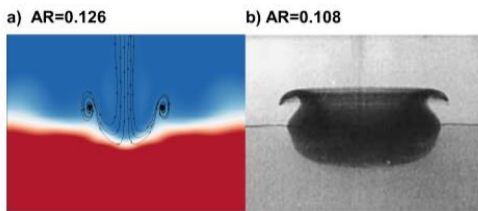


Fig. 6. Qualitative comparison with the experiments of Dahm *et al.*

3. 1 First Phase: Vortex formation

The initial development of three-dimensional vortex structures for three opening duration at various non-dimensionalized time instance ($t^* = tV_d / h$) is depicted in Fig. 7. Soon after the injection, the relatively cold fluid rolls-up and coherent vortical structures are formed near the inlet section. The evolution of three types of disturbances are analysed by plotting the contour of z vorticity ($\omega_z = \frac{\partial v}{\partial x} - \frac{\partial u}{\partial y}$) as shown in Fig. 7.

In case of relatively short opening duration, (weak disturbance) two isolated vortex rings are formed as shown in Fig. 7 (a). For medium disturbances, a short tail is formed behind the downward propagating primary vortex ring Fig. 7 (b). In case of large opening duration, (strong disturbance) the vortex

ring detachment phenomena was not observed as depicted in Fig. 7 (c). In this case, the disturbance fluid propagates as a jet-like structure rather than a vortex ring as observed in the other two cases.

A close up view of the vortex ring structure formed near the inlet port is shown in Fig. 8. The vortex ring displays as a vortex pair in the side view as observed in the two-dimensional simulations. The downward propagating vortex ring interacts with thermocline which is kept at the center of the TES.

3.2 Second phase: Impingement of coherent structures

In order to effectively understand the vortex ring-thermocline interaction mechanism, the collision of the coherent structures with three different stratification levels (different thermocline thickness) are systematically analysed.

3. 2. 1 Evolution of weak disturbance

The interface dynamics of weak disturbance with sharp, moderate and large interface are depicted in Fig. 9. The injected vortex ring propagates towards the thermocline and touches the upper layer of thermocline at $t^* \approx 1.42$. In case of sharp interface (SC1) the vortex ring barely penetrates the upper layer of the thermocline (Fig. 9 (a)). In this case the vortex ring thermocline interaction is analogous to vortex ring-wall interactions. With increase in flow time, the vortex ring spreads in the radial directions as shown in Fig. 9 (b).

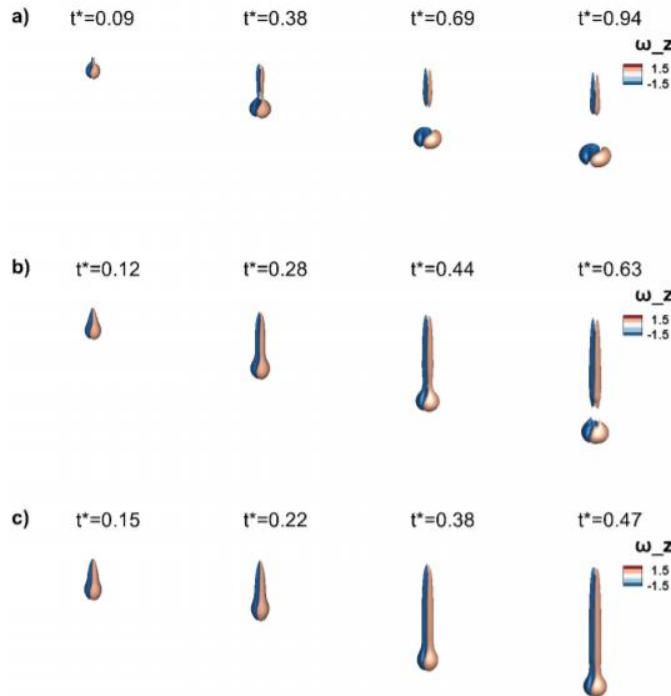


Fig. 7. Vorticity iso-surfaces at selected time instant ($\omega_z = \pm 1.5 s^{-1}$).

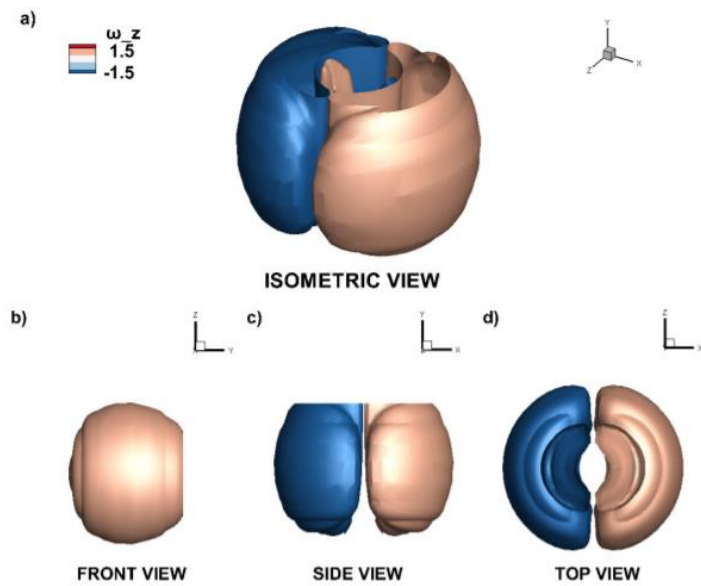


Fig. 8. Vortex ring (a) Isometric view, (b) Front View, (c) side view d) top view.

In the case of moderate interface, (MC1) the vortex ring partially penetrate the interface as shown in Figs. 9 (c) and (d).

In the case of large interface, (LC1) the vortex ring penetrates into thermocline cause oscillations in axial and radial directions. Baroclinic production of opposite signed vortices are observed in this case.

Here, a part of the vortex ring penetrates through the thermocline while the remainder recoils upward forming a plume structure (Figs. 9(e) and (f)) as in the experimental study of [Advaith et al. \(2017\)](#). Subsequently, the vortex ring shrinks in size and finally diffuses in the interface region. At later flow time, after a few rebounds, a new thermocline is established with increased thickness.

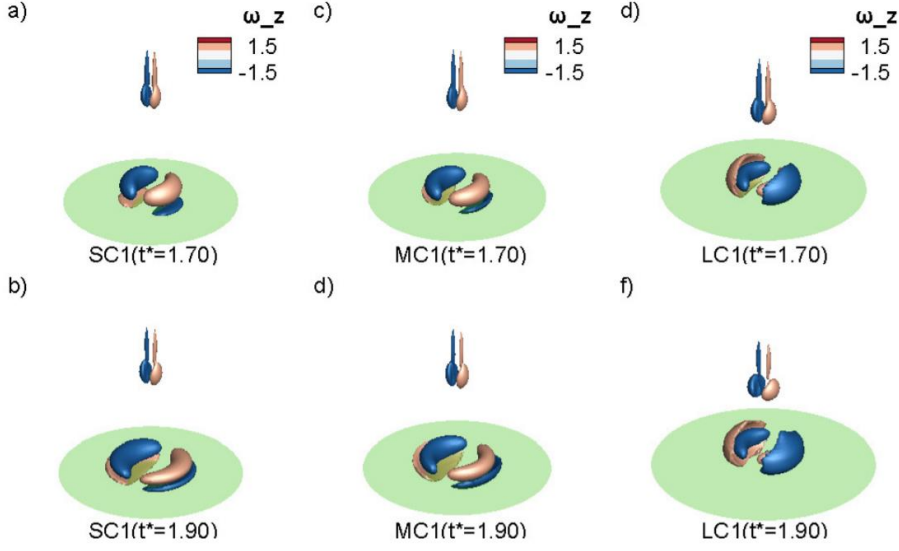


Fig. 9. Iso-surfaces of vorticity at two time instance: (a), (b) sharp interface; (c), (d) moderate interface; (e) and (f) large interface.

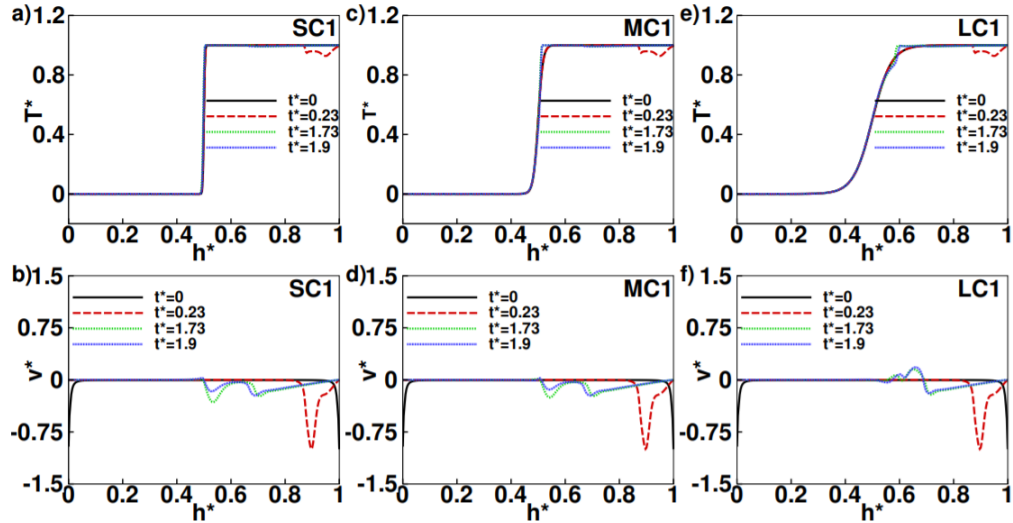


Fig. 10. Temperature and Velocity profile at center line at selected time instant a) $T^*(y)$ for sharp interface b) $v^*(y)$ for sharp interface c) $T^*(y)$ for medium interface d) $v^*(y)$ for medium interface e) $T^*(y)$ for strong interface f) $v^*(y)$ for strong interface.

Figure 10 shows the variation of temperature and velocity in axial direction at four time instants (at the center of the tank). The propagation of weak disturbance in the axial direction are evident in the temperature and velocity plots (Figs. 10 (a) and (b) respectively).

The upper part of the sigmoid profile is distorted by the flow disturbance. During initial stages ($t^* = 0.23$) the bulk of the inserted cold fluid (formed coherent structure) is at the top part of TES ($0.8 \leq h^* \leq 1$) which causes inflections in temperature and velocity profiles. At later flow time

the disturbance propagates downstream which alters the temperature and velocity profiles. Here, in the case of sharp interface, the disturbance is not strong to penetrate the top part of the interface. This is evident in the velocity profile graphs Fig. 10 (b). The axial profiles of temperature and velocity for moderate interface thickness case (MC1) are shown in Fig. 10 (c) and (d) respectively. Due to the addition of flow perturbations, the temperature profiles are initially distorted near the inlet and this distortion migrates downwards with increase in flow time. Distortions inside the thermocline region are evident in this case ($t^* = 1.9$).

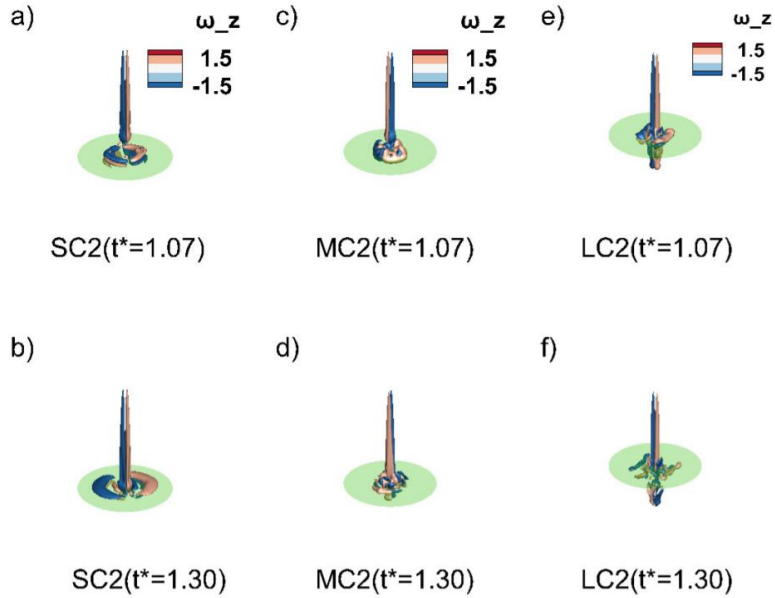


Fig. 11. Iso-surfaces of vorticity ($\omega_z = \pm 1.5 s^{-1}$) at two time instance (a) sharp interface, (b) Medium interface, (c) Large interface.

The velocity profiles (Fig.10 (d)) are qualitatively similar to SC1 case. In the case of large interface (LC1), some difference in the interaction mechanism are evident in the temperature and axial velocity profiles (Figs.10 (e) and (f)). Inflections inside the thermocline regions are observed in the case of large interface thickness (Fig. 10(e)). Positive values of axial velocity are observed in this case. This is related to the upward propagation of baroclinically generated plume- like structures.

3.2.2 Evolution of medium disturbance

Typical interface dynamics of medium disturbance with sharp, moderate and large interface are shown in Fig. 11. In the case of medium disturbances (SC2, MC2 and LC2) the interface dynamics is

complicated by the tail of the coherent structures. For Sc2 (sharp interface case), the vortex ring hardly penetrates and the interface remains flat after the impingement as shown in Fig. 11 (a). At later flow time, the disturbance propagates in the radial direction (Fig. 11 (b)). In the case of moderate interface thickness (MC2), multiple small scale structures are observed to orbit around the primary vortex ring near the interface as region as shown in Figs. 11 (c) and (d). Here, the spreading of the vorticity in the radial direction is less compared with SC2. In the case of large interface (LC2), the vortex ring -thermocline interaction creates a crater inside the thermocline region as shown in Fig. 11 (e) . The cold fluid stored in bottom half splashes upwards because of this interaction. Complex small scale structures are formed in the interface region due to the baroclinic generation of vorticity (Fig. 11 (f)).

In the case of moderate interface thickness, the partial penetration of disturbance is evident in the temperature profiles (Fig. 12 (c)). The velocity

profiles are quantitatively similar to weak disturbance cases as shown in Fig. 12 (d)). In the case of large interface thickness, the sigmoid profile is significantly disturbed by the impingement of vertical structure as shown in Fig. 12 (e)). Here, the complex interactions inside the thermocline creates multiple inflectional points in the velocity profiles (Fig. 12 (f)).

Here, the outer surface removal of the jet-like structure is reminiscent to the banana peeling process as observed in experimental study of [Shy \(1995\)](#).

Another important aspect of strong disturbance is the oscillations observed during the recovery phase (post impingement period) which will be discussed in the section 3.4.

Vorticity contour of strong disturbance with different interfaces are shown in Fig. 13. The temperature profiles shows negligible penetration for SC3 case (Fig. 14 (a)). For SC3 case increase in magnitude of velocity component is associated increase in the duration of flow disturbance (Fig. 14 (b)). Upward propagation of vortical structures are observed in the interface region for all the cases as evidenced in Figs. 14 (b) (d) and (f). In the case of moderate and large interface thickness (MC3 and LC3) a significant alteration in the sigmoid profiles are observed during the interaction period (Figs. 14 (c) and (e)).

3.3 Third phase: Thermocline oscillations and Spectra

During the post-impingement period (recovery phase), continuous damping oscillations of thermocline are observed in the simulation. Thermocline oscillations are observed for all the simulation cases. However, the amplitude of oscillations is highest for strong disturbances cases.

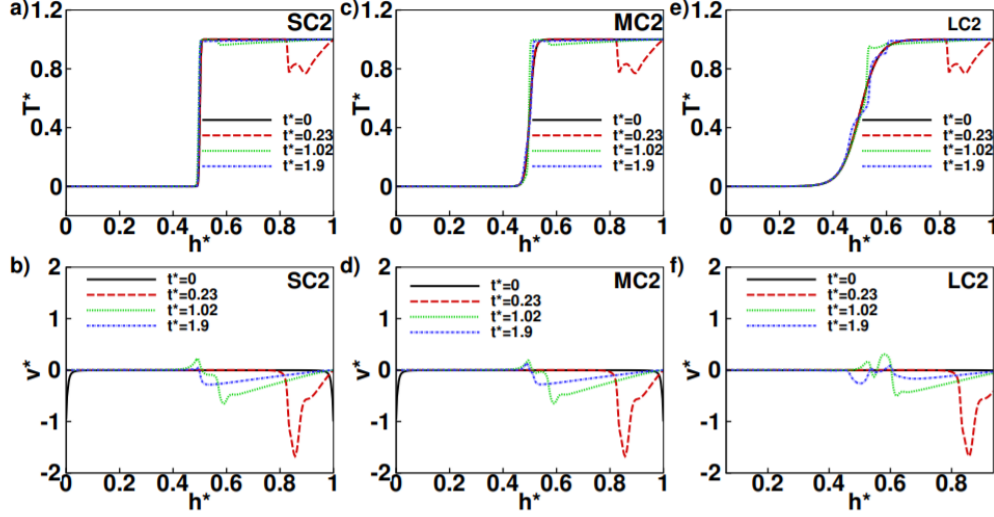


Fig. 12. Temperature and Velocity profile at center line at selected time instant (a) $T^*(y)$ for sharp interface, (b) $v^*(y)$ for sharp interface, (c) $T^*(y)$ for medium interface, (d) $v^*(y)$ for medium interface, (e) $T^*(y)$ for strong.

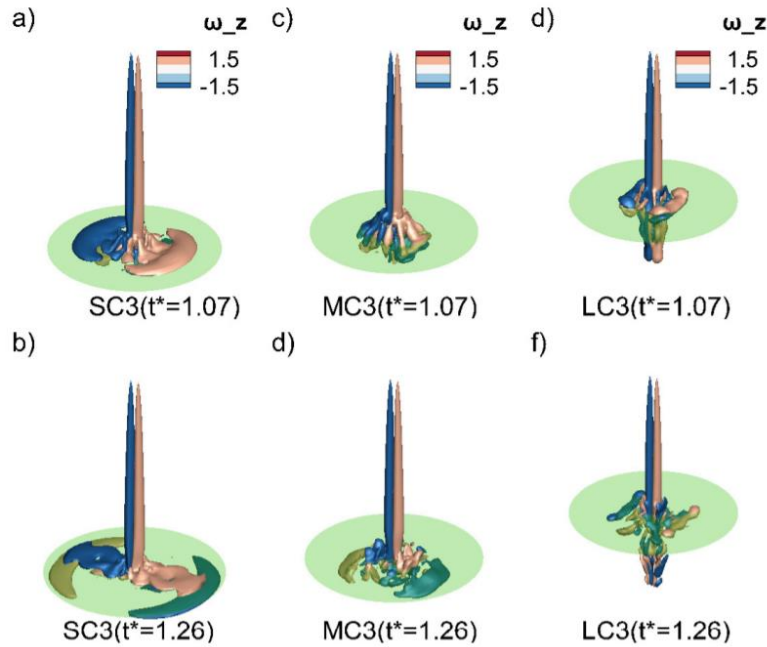


Fig. 13. Iso-surfaces of vorticity($\omega_z = \pm 1.5 s^{-1}$) at two time instance a) sharp interface b)Medium interface c)Large interface.

In order to quantify the nature of oscillations temporal variation of axial and radial velocity and the corresponding spectra at the center of the thermocline are plotted in Figs. 15 and 16. Here, the amplitude of oscillations decreases with increase in thermocline thickness as shown in Fig. 15. The obtained peak frequency from the FFT analysis scales with the buoyancy frequency (Brunt-Väisälä frequency). Brunt-Väisälä frequency is tabulated in table 2.

In order to understand the flow dynamics during the thermocline oscillations phase, the vorticity plot during one cycle is plotted in Fig. 17. Here, the thermocline oscillations near the thermocline region is connected with the generation of baroclinic vorticity. Figure 17 indicates that the oscillations at the interface are through the successive generation of countersign vorticity which retards/suppresses the propagation of the disturbance.

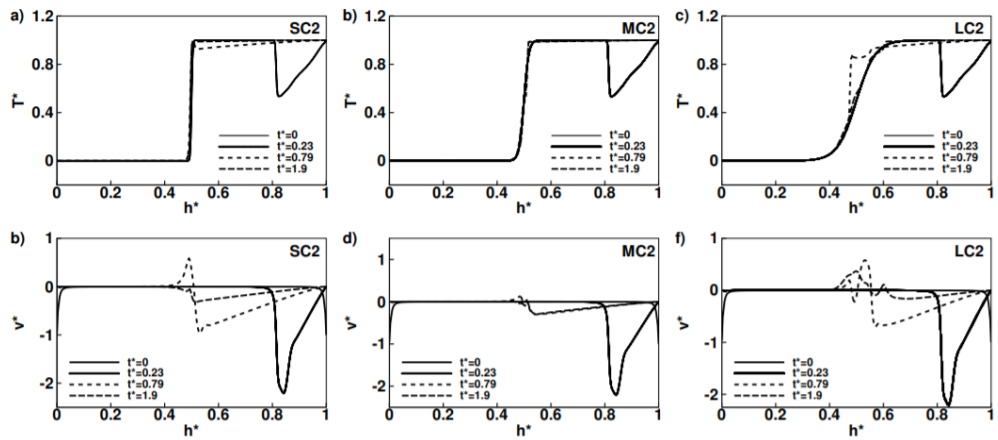


Fig. 14. Temperature and Velocity profile at center line at selected time instant (a) $T^*(y)$ for sharp interface, (b) $v^*(y)$ for sharp interface, (c) $T^*(y)$ for medium interface, (d) $v^*(y)$ for medium interface, (e) $T^*(y)$ for strong interface, (f) $v^*(y)$ for strong interface.

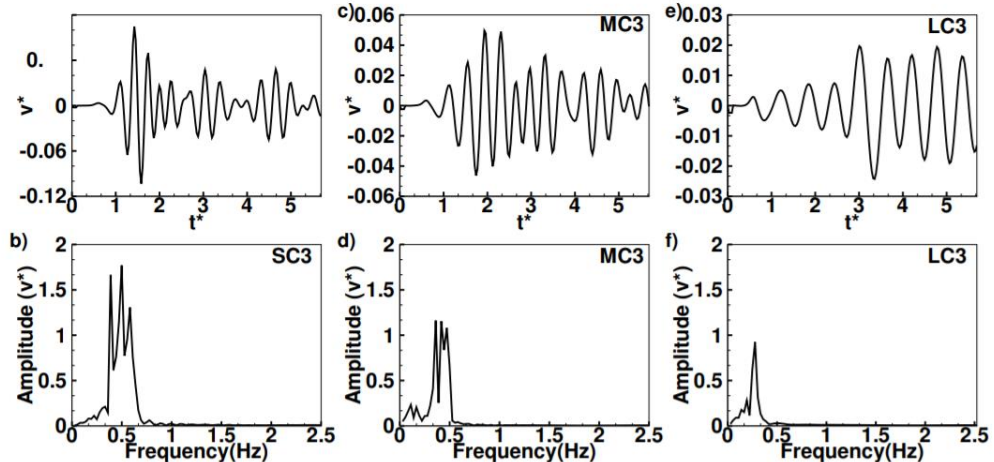


Fig. 15. Temporal variation of axial velocity and spectra.

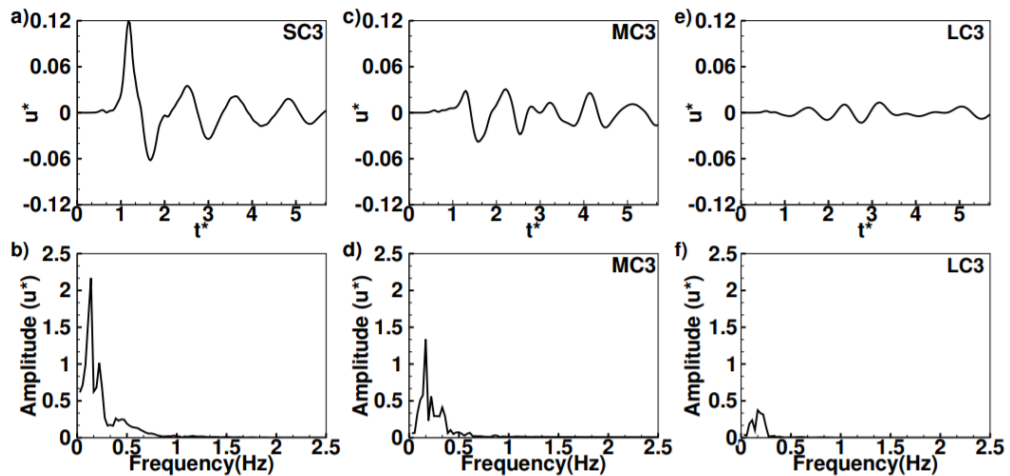


Fig. 16. Temporal variation of radial velocity and spectra.

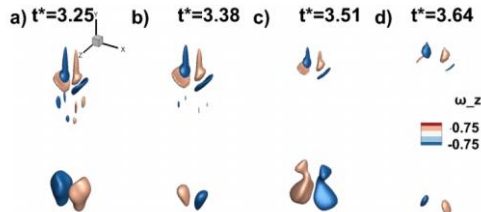


Fig. 17. Vorticity production at the interface.

Table 2 Parameters of under-damped oscillations induced by flow disturbance at $r^*=0$, $h^*=0.5$

Case	Brunt-Väisälä frequency	Peak frequency
SC3	1.09	0.4991
MC3	0.64	0.3605
LC3	0.33	0.2772

For large interface case the internal waves are generated by the periodic array of vortices which generates a standing wave pattern near the Brunt-Väisälä frequency.

4. CONCLUSIONS

Three-dimensional numerical studies of propagation of external flow disturbances and associated mixing dynamics in a scaled down thermally stratified storage tank are carried out for three inlet perturbations. The temporal evolution of these disturbances and the subsequent interaction with different interface thickness are systematically analysed. Computations have shown that the evolution of the flow disturbance consists of three distinct phases. During the initial development phase, the weak disturbance rolls-up in to a vortex ring near the inlet port, whereas in the case of medium and strong disturbance cases, the detachment phenomena of vortex rings were not observed. The injected fluid propagates as a jet-like structure and impinges on the thermocline. During the second phase, a wide gamut of flow structures are observed near the thermocline region depending upon the interface thickness and strength of the disturbance. In the case of sharp interfaces, the interface acts as a barrier and the disturbance fluid barely penetrates the interface. The disturbance penetrates the thermocline and spread in the radial direction for medium disturbance case. In case of large interface thicknesses, the disturbance fluid smoothly penetrated the interface with negligible radial spreading, especially for strong disturbances. Subsequently, during the final recovery phase, periodic thermocline oscillations are observed in axial and radial directions. Finally, the abrupt mixing and thermocline oscillations come to rest and a new stable thermocline is formed for any kind of disturbance. However, the extent of mixing in the region of thermocline dictates the formation of new thermocline and the oscillation frequency.

REFERENCES

- Advaith, S., K. Manu, A. Tinaikar, U. K. Chetia and S. Basu (2017). Interaction of vortex ring with a stratified finite thickness interface. *Physics of Fluids* 29(9), 093602.
- Advaith, S., D. R. Parida, K. Aswathi, N. Dani, U. K. Chetia, K. Chattopadhyay and S. Basu (2021). Experimental investigation on single-medium stratified thermal energy storage system. *Renewable Energy* 164, 146–155.
- Dahm, W., C. Scheil and G. Tryggvason (1989). Dynamics of vortex interaction with a density interface. *Journal of Fluid Mechanics* 205, 1–43.
- Flueckiger, S. M., Z. Yang and S. V. Garimella (2013). Review of molten-salt thermocline tank modeling for solar thermal energy storage. *Heat Transfer Engineering* 34(10), 787–800.
- Gil, A., M. Medrano, I. Martorell, A. Lázaro, P. Dolado, B. Zalba and L. F. Cabeza (2010). State of the art on high temperature thermal energy storage for power generation. part 1concepts, materials and modellization. *Renewable and Sustainable Energy Reviews* 14(1), 31–55.
- González-Roubaud, E., D. Pérez-Osorio and C. Prieto (2017). Review of commercial thermal energy storage in concentrated solar power plants: Steam vs. molten salts. *Renewable and Sustainable Energy Reviews* 80, 133–148.
- Hatte, S., C. Mira-Hernández, S. Advaith, A. Tinaikar, U. K. Chetia, K. Manu, K. Chattopadhyay, J. A. Weibel, S. V. Garimella, V. Srinivasan, et al. (2016). Short and longterm sensitivity of lab-scale thermocline based thermal storage to flow disturbances. *Applied Thermal Engineering* 109, 936–948.
- Kearney, D., U. Herrmann, P. Nava, B. Kelly, R. Mahoney, J. Pacheco, R. Cable, N. Potrovitz, D. Blake and H. Price (2003). Assessment of a molten salt heat transfer fluid in a parabolic trough solar field. *Journal of Solar Energy Engineering* 125(2), 170–176.
- Linden, P. (1973). The interaction of a vortex ring with a sharp density interface: a model for turbulent entrainment. *Journal of Fluid Mechanics* 60(3), 467–480.
- Manu, K., P. Anand, U. K. Chetia and S. Basu (2015). Effects of instabilities and coherent structures on the performance of a thermocline based thermal energy storage. *Applied Thermal Engineering* 87, 768–778.
- Manu, K., P. Deshmukh and S. Basu (2016). Rayleigh–taylor instability in a thermocline based thermal storage tank. *International Journal of Thermal Sciences* 100, 333–345.
- Medrano, M., A. Gil, I. Martorell, X. Potau and L. F. Cabeza (2010). State of the art on high-temperature thermal energy storage for power

- generation. part 2case studies. *Renewable and Sustainable Energy Reviews* 14(1), 56–72.
- Olsthoorn, J. and S. Dalziel (2017). Three-dimensional visualization of the interaction of a vortex ring with a stratified interface. *Journal of Fluid Mechanics* 820, 549–579.
- Orlandi, P., P. Egermann and E. Hopfinger (1998). Vortex rings descending in a stratified fluid. *Physics of Fluids* 10(11), 2819–2827.
- Qin, F. G., X. Yang, Z. Ding, Y. Zuo, Y. Shao, R. Jiang and X. Yang (2012). Thermocline stability criterions in single-tanks of molten salt thermal energy storage. *Applied Energy* 97, 816–821.
- Reddy, R. G. (2011). Molten salts: thermal energy storage and heat transfer media. *Journal of Phase Equilibria and Diffusion* 32(4), 269–70.
- Shaikh, W., A. Wadegaonkar, S. Kedare and M. Bose (2018). Numerical simulation of single media thermocline based storage system. *Solar Energy* 174, 207–217.
- Shy, S. (1995). Mixing dynamics of jet interaction with a sharp density interface. *Experimental Thermal and Fluid Science* 10(3), 355–369.
- Suresh, C. and R. P. Saini (2020). Review on solar thermal energy storage technologies and their geometrical configurations. *International Journal of Energy Research* 44(6), 4163–4195.
- Tinaikar, A., S. Advaith, U. K. Chetia, K. Manu and S. Basu (2016). Spatio-temporal disruption of thermocline by successive laminar vortex pairs in a single tank thermal energy storage. *Applied Thermal Engineering* 109, 924–935.
- Van Berkel, J., C. Rindt and A. Van Steenhoven (2002). Thermocline dynamics in a thermally stratified store. *International Journal of Heat and Mass Transfer* 45(2), 343–356.
- Xu, C., Z. Wang, Y. He, X. Li and F. Bai (2012). Sensitivity analysis of the numerical study on the thermal performance of a packed-bed molten salt thermocline thermal storage system. *Applied Energy* 92, 65–75.
- Yang, Z. and S. V. Garimella (2010). Molten-salt thermal energy storage in thermoclines under different environmental boundary conditions. *Applied Energy* 87(11), 3322–3329.
- Yuan, F., M.-J. Li, Z. Ma, B. Jin and Z. Liu (2018). Experimental study on thermal performance of high-temperature molten salt cascaded latent heat thermal energy storage system. *International Journal of Heat and Mass Transfer* 118, 997–1011.
- Zachar, A., I. Farkas and F. Szlivka (2003). Numerical analyses of the impact of plates for thermal stratification inside a storage tank with upper and lower inlet flows. *Solar Energy* 74(4), 287–302.